Accepted Manuscript

Multifunctional Dy (III) doped di-calcium silicate array for boosting display and forensic applications

M. Venkataravanappa, R.B. Basavaraj, G.P. Darshan, B. Daruka Prasad, S.C. Sharma, P. Hema Prabha, S. Ramani, H. Nagabhushana

Please cite this article as: Venkataravanappa M, Basavaraj RB, Darshan GP, Prasad BD, Sharma SC, Hema Prabha P, Ramani S, Nagabhushana H, Multifunctional Dy (III) doped di-calcium silicate array for boosting display and forensic applications, *Journal of Rare Earths* (2018), doi: 10.1016/j.jre.2017.11.013.

Multifunctional Dy (III) doped di-calcium silicate array for boosting display and forensic applications

M. Venkataravanappa[1, 2], R.B. Basavaraj[3], G.P. Darshan[4], B. Daruka Prasad[5], S.C. Sharma[6, 7], P. Hema Prabha[8], S. Ramani[8], H. Nagabhushana[3, *]

[1]Department of Physics, Govt. First Grade College, Sira, Tumkur 572 137, India
[2]Research and Development Center, Bharathiar University, Coimbatore 641 046, India
[3]Prof. C.N.R. Rao Centre for Advanced Materials Research, Tumkur University, Tumkur 572 103, India
[4]Department of Physics, Acharya Institute of Graduate Studies, Bangalore 560 107, India
[5]Department of Physics, BMS Institute of Technology and Management, VTU-affiliated, Bangalore 560 064, India
[6]Department of Mechanical Engineering, Jain University, Advisor, Jain group of Institutions, Bangalore 560 069, India
[7]Advisor, Avinashilingam Institute for Home Science and Higher Education for Women University, Coimbatore 6410 43, India
[8]Department of Food Processing and Preservation Technology, Avinashilingam Institute for Home Science and Higher Education for Women University, Coimbatore 641 043, India

Abstract

Latent fingerprints (LFPs) are the major physical evidences for identification of individuals during crime spot investigation. Till date, numerous methods were followed to visualize LFPs. However, simple, accurate, and cost-effective method has wide scope in advanced forensic field. In our work, Ca_2SiO_4:Dy^{3+} nanopowders (NPs) were fabricated via solution combustion route. The optimized sample was employed for visualization of overlapped LFPs by following cost effective powder dusting method. The obtained results reveal complete three levels of ridge characteristics with high sensitivity, reproducibility, selectivity, and reliability on various complex surfaces. The photoluminescence (PL) spectra consist of intense peaks at ~ 480 and 574 nm owing to $^4F_{9/2} \rightarrow ^6H_{15/2}$ and $^4F_{9/2} \rightarrow ^6H_{13/2}$ 4f transitions of Dy^{3+} ions, respectively. The photometric properties confirm that the samples exhibit intense white emission with high color purity. Therefore, the present prepared NPs could be a definitive choice as advanced luminescent NPs for forensic, solid state lighting and portable FED devices.

*Corresponding Author: E-mail address: bhushanvlc@gmail.com (Dr. H. Nagabhushana).

1. Introduction

White light-emitting diodes (WLEDs) have emerged as next generation illumination technology. The WLEDs create numerous interest for research community due to their high luminous efficiency, long lifetime, energy saving, harmlessness, easy fabrication, high stability and environmental safety [1-3]. Recently, much research has been carried out to enhance the efficiency of new generation WLEDs. Thus, rare earth (RE) ions activated phosphors have attracted much attention of many scientists due to their unique electronic, optical and chemical properties that construct the phosphors constructive wide spread of applications, namely, laser materials, optical amplifiers, photocatalysts, sensors and anti-counterfeiting inks [4]. Therefore, the trivalent RE ions doped crystalline hosts are receiving more attention as optical materials emitting which are capable to emit in visible and near-IR regions [5].

Among many RE ions, Dy^{3+} ions are extensively investigated because it provides two typical emission bands in blue (480 nm) and yellow (570 nm) regions, which are essential for full color displays [6-8]. In addition, through appropriate tuning of yellow-to-blue (Y/B) emission intensity, it was likely to achieve pure white light emission from Dy^{3+} doped nanophosphors. Therefore, it was interesting to study the luminescence properties of Dy^{3+} in different host lattices.

Silicates are considered to be the best host materials for luminescence centers due to their excellent chemical and thermal stability, long persistence time, better formability, multicolor phosphorescence, easy preparation, resistance for alkali and oxygen [9]. The RE or transition metal ions doped silicates has been of great interest for researchers stemming from their intense luminescence emission in blue, green and red emission regions [10-12]. However, fabrication of nanophosphors followed by improved techniques creates wide applications. The variety of

methods were designed, including templating method, sol-gel reaction, sonochemical, solution combustion route, and etc. [13-16]. Among the reported synthesis techniques, the solution combustion route was a low-cost, time saving and high-yield approach.

Fingerprints (FPs) were considered to be a vital source for identification of individuals in advanced forensic investigation. The ridge patterns on the tips of human fingers were unique and remain the same throughout lifespan. Most commonly found FPs during crime spot investigation was latent; as a result efficient methods were necessary to visualize such as LFPs [17-19]. Till date, numerous methods (chemical, optical) have been established to visualize LFPs. However, most of the followed techniques have several drawbacks, such as low sensitivity, high background hindrance, complicated procedure, high toxicity and their visualization restricted only levels 1 and 2 ridge details due to poor image qualities. These ridge details were easily forged by artificial skin imprints. Therefore, the visualization of level 3 ridge characteristics would necessitate overcoming such artificial FPs anti-counterfeiting and it creates numerous interests for researchers [20].

Nanosized particles with spherical morphology were considered to be an innovative advancement for visualization of LFPs in powder dusting method. It offers superior sensitivity, little background hindrance, extraordinary efficiency, lesser toxicity and stress-free detection of LFPs, which was the essential requirement for forensic investigators [21]. Further, many researches have been available in the literature for the visualization of LFPs by making use of NPs by exciting with ultraviolet (UV) radiation. The UV light has many drawbacks including high background interference owing to the significant auto-fluorescence from the substrates, photo damage to the skin and eyes of the operators, and the possibility of severe irradiation-induced damage. Therefore, NPs which can reveal well defined level 3 ridge details under normal light have wide scope of applications in the field of forensic science [22].

In our present work, novel $Ca_2SiO_4:Dy^{3+}$ (1 mol%–11 mol%) NPs were fabricated by bio-inspired simple solution combustion route. The optimized sample was explored as a novel labeling agent for LFPs visualization on various porous and non porous surfaces under normal white light.

2. Experimental

2.1. Materials and methods

Solution combustion route was employed for the fabrication of $Ca_2SiO_4:Dy^{3+}$ (1 mol%–11 mol%) NPs. The starting materials used for the preparation were calcium nitrate tetrahydrate ($Ca(NO_3)_2\cdot 4H_2O$; Sigma-Aldrich; 99%), dysprosium nitrate ($Dy(NO_3)_3\cdot H_2O$; Sigma-Aldrich; 99%) and fumed silica source as an oxidizer and oxalyl dihydrazide (ODH: $C_2H_6N_4O_2$) was used as a fuel. The stoichiometric quantities of oxidizers and fuel were thoroughly mixed in double distilled water using a magnetic stirrer. The clear solution was placed into a pre-heated muffle furnace maintained at $\sim 500 \pm 10$ ^{o}C. Initially, the solution was thermally dehydrated and ignited with the liberation of large amount of gases (N_2, O_2, etc.). After the completion of process, the product was obtained and calcined at ~ 950 ^{o}C for ~ 3 h. The schematic illustration for the synthesis of $Ca_2SiO_4:Dy^{3+}$ (1 mol%–11 mol%) NPs is shown in Fig. 1.

2.2. Characterization

The powder X-ray diffraction (PXRD) measurements were recorded using Shimadzu made model-7000, having a high precision vertical θ–θ goniometry at a wavelength of 0.154 nm. Morphology and size of the NPs were examined by scanning electron microscopy (SEM, Hitachi-3000) and transmission electron microscopy (TEM, TECNAI F-30). Diffuse reflectance (DR) spectroscopy of the samples was recorded on a Perkin Elmer (Lambda-35) spectrometer. Photoluminescence (PL) measurements were carried out using a Horiba Fluorolog-3, modular Spectroflourimeter.

2.3. Visualization of LFPs by staining $Ca_2SiO_4:Dy^{3+}$ (3 mol%) NPs

All the LFPs were collected from single donor of age 26 years old male. The hands of the donor were thoroughly washed with soap and cleaned with water, propanol, and ethanol. Then, washed hands were dried in air, gently rubbed on forehead and deposited on various forensic related surfaces. The optimized $Ca_2SiO_4:Dy^{3+}$ (3 mol%) NPs were carefully stained on LFPs and excess powder was removed by smooth brushing method. The visualization of fingerprint images were recorded under normal light by using a 50 mm f/2.8G ED lens Nikon D3100/AF-S digital camera. Fig. 2. shows the pictorial representation of visualization of LFPs stained by $Ca_2SiO_4:Dy^{3+}$ (3 mol%) NPs by powder dusting method. The superiority of visualized FPs on various porous and non-porous surfaces was evaluated by using Bandey's scale developed by UK Home Office. This five point scale system was extensively used to estimate the quality of fingerprints only in research circumstance instead of in legal procedures (Table 1). According to Bandey's system, grade 3 or grade 4 fingerprints were considered for explicit identification of individuals.

3. Results and discussion

Fig. 3(a) shows the PXRD profiles of pure and Dy^{3+} (1 mol%–11 mol%) doped Ca_2SiO_4 NPs. Intense diffraction peaks belonging to monoclinic system (JCPDS No. 84-0655) of $Ca_2SiO_4:Dy^{3+}$ was observed. The PXRD patterns of the doped samples resembles with the undoped sample. In the unit cell of perovskite Ca_2SiO_4, Si^{4+} ions are positioned at the center of a cube; O^{2-} ions are positioned at six-face centers of the cube and Ca^{2+} ions were positioned at the eight apex angles of cube. Octahedrons were made up of Si^{4+} ions and the nearest neighbor O^{2-} ions and its coordination number is six. Icosahedrons were made up of Ca^{2+} ions and the nearest neighbor O^{2-} ions and the co-ordination number are twelve. The co-ordination numbers of the both Si^{4+} ions and Ca^{2+} ions were eight [23]. As the Dy^{3+} concentration increases, no significant changes were observed up to 5 mol% and thereafter small impurity peak of Dy_2O_3 was observed at ~ $2\theta=36°$ (Fig. 3(a)). This indicates that the Dy^{3+} ions are effectively substituted in the Ca^{2+} site in the host.

The average crystallite sizes of pure and $Ca_2SiO_4:Dy^{3+}$ (1 mol%–11 mol%) NPs were determined by both Scherrer's relation and Williamson - Hall plots [24].

$$D = \frac{0.9\,\lambda}{\beta\cos\theta} \quad \text{--- (1)}$$

where 'β' denotes the diffracted full width at half maximum (FWHM in radian) caused by the crystallites, 'λ' the wavelength of X-ray (0.1542 nm), 'θ' the Bragg angle and k; the constant depending on the grain shape (0.90). The W – H approach considers the case when the domain effect and lattice deformation were both simultaneously operative and their combined effects give the final line broadening FWHM (β), which was the sum of grain size and lattice distortion. This relation assumes a negligibly small instrumental contribution compared with the sample – dependent broadening. W–H equation may be expressed in the form:

$$\beta\cos\theta = \varepsilon\left(4\sin\theta\right) + \frac{\lambda}{D} \text{------------------------------- (2)}$$

where 'β' (FWHM in radians) stands for different XRD lines corresponding to different planes, ε the strain developed and D the grain size. The W-H plots of $Ca_2SiO_4:Dy^{3+}$ (1 mol%–11 mol%) NPs are shown in Fig. 3(b). The slope of the straight line gives the strain (ε) and intercept (λ / D) on the Y - axis gives crystallite size (D). The other structural parameters namely dislocation density (δ) and stacking fault (SF) were determined using the following relation:

$$\delta = \frac{1}{D^2} \qquad (3)$$

$$SF = \left[\frac{2\pi^2}{45\left(3\tan\theta\right)^{1/2}} \right] \text{----------------------------- (4)}$$

The estimated average crystallite size, strain, dislocation density and stacking fault for host and $Ca_2SiO_4:Dy^{3+}$ (1 mol%–11 mol%) NPs are tabulated in Table 2. It was evident that, the crystallite size estimated from W- H plots was slightly higher than those calculated using Scherrer's formula. The small variation in the values was due to the fact that in Scherrer's formula strain component was assumed to be zero and observed broadening of diffraction peak was considered as a result of reducing grain size only.

Figs. 4(a–f) show the SEM micrographs of $Ca_2SiO_4:Dy^{3+}$ (1 mol%–11 mol%) NPs. Irregular shape was observed for the prepared samples due to uneven distribution of temperature and mass flow in the combustion flame. Further, more pores nature was revealed attributed to gases that escape with high pressure during combustion. This type of porous network was typical and commonly observed in combustion synthesis [25]. Fig. 4(g, h) show the TEM and HRTEM images of the optimized $Ca_2SiO_4:Dy^{3+}$ (3 mol%) NPs. From HRTEM image, it can be clearly seen that the lattice fringes with the interplanar spacing (d) of ~ 0.32 nm corresponds to (302) plane. The observed diffraction spot in SAED pattern indicates the formation of semi crystalline NPs of the samples (Inset Fig. 4(h)).

Diffuse reflectance spectra (DRS) of pure and Dy^{3+} (1 mol%–11 mol%) doped Ca_2SiO_4 NPs recorded in the range of 200 – 1100 nm at RT are shown Fig. 5(a). The spectra exhibits peaks at ~ 320, 348, 364, 381, 796, 887 and 1071 nm which were attributed to $^6H_{15/2} \to {}^4I_{11/2}$, $^6H_{15/2} \to {}^6P_{7/2}$, $^6H_{15/2} \to {}^4I_{13/2}$, $^6H_{15/2} \to {}^6F_{5/2}$, $^6H_{5/2} \to {}^6F_{7/2}$ and $^6H_{5/2} \to {}^6F_{9/2} + {}^6H_{7/2}$ respectively. The red shifting of bands in the DRS was also observed due to the variation in the crystallite size and increase of dysprosium ions into the host matrix. Fig. 5(b) shows the magnified view of Dy^{3+} peaks centered at 796 and 887 nm which were attributed to $^6H_{15/2} \to {}^6F_{5/2}$ and $^6H_{15/2} \to {}^6F_{7/2}$ respectively.

The Kubelka-Munk (K-M) theory [26] was employed to evaluate the energy band gaps of $Ca_2SiO_4:Dy^{3+}$ (1 mol%–11 mol%) NPs using DR spectra as shown in Fig. 5(c). The Kubelka-Munk function $F(R_\infty)$ and band gap energy ($h\nu$) were estimated by utilizing the following equations:

$$F(R_\infty) = \frac{(1 - R_\infty)^2}{2R_\infty} \text{-------------------- (5)}$$

$$h\nu = \frac{1240}{\lambda} \text{-------------------- (6)}$$

where R_∞, represents reflection coefficient of the sample and λ the absorption wavelength. The decrease of energy band gap (5.19 – 5.30 eV) with increase of the dopant (Dy^{3+}) concentration was observed and is shown in Figs.5 (c, d). Variation of energy band gap with dopant concentration was due to the fact that shallow level donor impurities create energy levels in the band gap near the conduction band edge and shallow acceptor impurities create energy levels near the valence band edge. With increase in the amount of doping, the density of states of these dopants increases and forms a continuum of states as the band gap decreases [27].

The PL excitation spectrum of $Ca_2SiO_4:Dy^{3+}$ (3 mol%) NPs under 574 nm excitation wavelengths is shown in Fig.6 (a). The spectrum consists of a peaks at ~ 230, 350, 365, 380, 420 and 455 nm corresponding to $^6H_{15/2} \rightarrow ^6P_{3/2}$, $^6H_{15/2} \rightarrow ^6P_{7/2}$, $^6H_{15/2} \rightarrow ^6P_{5/2}$, $^6H_{15/2} \rightarrow ^4I_{13/2}$, $^6H_{15/2} \rightarrow ^4G_{11/2}$ and $^6H_{15/2} \rightarrow ^4I_{15/2}$ transition of Dy^{3+} ions. The PL emission spectra of $Ca_2SiO_4:Dy^{3+}$ (1 mol%–11 mol%) NPs under 350 nm excitation wavelength at RT are shown in Fig.6 (b). The spectra reveal intense peaks at ~ 480, 574 and 666 nm which were attributed to the $^4F_{9/2} \rightarrow ^6H_J$ (J = 15/2, 13/2 and 11/2) transitions, respectively [28]. Among these, peaks at ~ 574 nm and 480 nm belong to purely electric dipole (ED) and magnetic dipole (MD) transitions respectively. The ED transition was very sensitive to the crystal field while MD transition does not change with the host environment significantly. The emission intensity was increased with increase of Dy^{3+} concentration upto 3 mol% and afterwards decreases (Fig.6 (c)) due to concentration quenching phenomena. The critical distance (R_c) between the two neighboring activator ions was estimated using structural parameters namely unit cell volume (V), Dy^{3+} sites per unit cell (N) and critical Dy^{3+} concentration (X_c) [29].

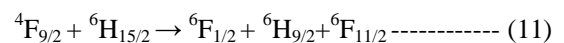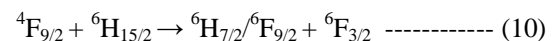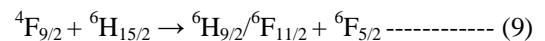$$R_c \approx 2 \left[\frac{3V}{4X_c \pi N} \right]^{1/3} \text{----------------- (7)}$$

In the present phosphor, N = 4, V = 0.786 nm^3 and X_c = 0.03. The estimated value of R_c was found to be ~ 1.024 nm and was higher than 0.5 nm. Fig. 6(d) shows the possible mechanism for the concentration quenching phenomena in $Ca_2SiO_4:Dy^{3+}$ NPs. It implies that the non-radiative energy transfer was responsible for energy transfer among Dy^{3+} ions due to multipole - multipole interaction. According to Van Uitert's, the multipolar interaction can be estimated by utilizing the following relation [30]:

$$\frac{I}{x} = \frac{K}{\beta(x)^{\frac{Q}{3}}} \text{--------------- (8)}$$

where I/x stand for the emission intensity (I) per dopant ion (x) concentration, and Q stand for the type of interaction between the dopant ions having values 6, 8 and 10 demonstrating exchange interactions, dipole-dipole (d–d), dipole-quadrupole (d-q) and quadrupole-quadrupole (q–q) interactions respectively. K and β are the constants. A logarithmic plot of (I/x) vs (x) was fitted to provided slope (–$Q/3$) value to be ~ –1.365 (Fig. 6(e)). The estimated value of Q was found to be ~ 7.28 which was nearest to theoretical value of 6. This entails that the d–d interactions was responsible for the concentration quenching.

Considering the energy match rule, the following cross-relaxation channels (CRC1, CRC2 and CRC3) among Dy^{3+} are responsible for population decrease of $^4F_{9/2}$ level [31]:

$$^4F_{9/2} + {}^6H_{15/2} \rightarrow {}^6H_{9/2}/{}^6F_{11/2} + {}^6F_{5/2} \text{------------ (9)}$$

$$^4F_{9/2} + {}^6H_{15/2} \rightarrow {}^6H_{7/2}/{}^6F_{9/2} + {}^6F_{3/2} \text{------------ (10)}$$

$$^4F_{9/2} + {}^6H_{15/2} \rightarrow {}^6F_{1/2} + {}^6H_{9/2} + {}^6F_{11/2} \text{------------ (11)}$$

The excitation energy of Dy^{3+} ion present in excited state transferred to neighboring ions and promotes the latter from the ground state to the metastable level. The Dy^{3+} ions at $^4F_{9/2}$ level was de-excited via these three cross-relaxation

processes while the ground state Dy^{3+} ions will accept the energies from the Dy^{3+} at $^6H_{15/2}$ level simultaneously. Finally, all the Dy^{3+} ions will go in their ground states and thus the luminescence related to $^4F_{9/2}$ level was quenched. The possible energy level diagram of Dy^{3+} ions in Ca_2SiO_4 host is shown in Fig. 6(f).

Commission International de I'Eclairage (CIE) 1931 (x-y) chromaticity diagram of Ca_2SiO_4:Dy^{3+} (1–11 mol%) NPs is depicted in Fig. 7(a). As shown in figure the CIE chromaticity co-ordinates were located in the white region. Fig. 7(b) shows the CCT diagram of Ca_2SiO_4:Dy^{3+} (1 mol%–11 mol%) NPs excited under 350 nm. The CCT was a specification of the color appearance of the light emitted by a light source, relating its color to the color of light from a reference source when heated to a particular temperature. However, lamps with a CCT rating below 3200 K was usually considered as "warm" light sources, while those with a CCT above 4000 K was usually considered as "cool" in appearance [32]. In the present study, the average CCT value of Ca_2SiO_4:Dy^{3+} (1 mol%–11 mol%) NPs was found to be ~ 6151 K which was well acceptable range of vertical cool daylight. Thus, the present phosphor was quite useful for artificial production of illumination devices.

Color purity of the sample was calculated using the relation:

$$\text{color purity} = \frac{\sqrt{(x_s - x_i)^2 + (y_s - y_i)^2}}{\sqrt{(x_d - x_i)^2 + (y_d - y_i)^2}} \times 100\% \ - - - - - (12)$$

where, (x_s, y_s) are the co-ordinates of a sample point, (x_d, y_d) the co-ordinates of the dominant wavelength, and (x_i, y_i) the co-ordinates of the illuminant point [33]. The dominant wavelength point can be calculated from the intersection point of the connecting line between equal energy point and sample point. The color purity of prepared NPs was found to be in the range of 80% to 85%, which was very close to the standard white light source.

Further, quantum efficiency (QE) of the prepared samples was estimated by the relations as follows [34, 35]:

$$QE = \frac{\text{Number of photons emitted}}{\text{Number of photons absorbed}} = \frac{E_c - E_a}{L_a - L_c} \quad \text{---------- (13)}$$

where, E_C and E_a are integrated luminescence of the phosphor and empty integrating sphere (blank), respectively, L_a denotes the integrated excitation profile from the empty integrating sphere, L_c is the integrated excitation profile when the sample was directly excited by the incident beam. The QE of the prepared samples were estimated and listed in Table 3. As can be evidenced from the table, the highest QE was found to be ~ 82.88 %. Therefore, the present prepared NPs could be a definitive choice as advanced luminescent NPs for solid state lighting and portable FED devices.

The Judd-Ofelt (J-O) theory has been applied to understand the environment on the site symmetry as well as effect of Dy^{3+} ions in Ca_2SiO_4 host. The J-O parameters (Ω_2 and $\Omega_{4,6}$) depend on asymmetric nature of the activator Dy^{3+} ligand and long range effects. The detailed procedure was described elsewhere [36]. The relation between radiative emission rates and integrated emission intensities can be expressed by relation [37];

$$\frac{A_{0-2,4}}{A_{0-1}} = \frac{I_{0-2,4}}{I_{0-1}} = \frac{h\upsilon_{0-1}}{h\upsilon_{0-2,4}} \quad \text{----------------- (14)}$$

where I_{0-J} and $h\upsilon_{0-J}$ stand for integrated emission intensity and energies corresponding to transitions $^4F_{9/2} \rightarrow ^6H_J$ (J = 15/2, 13/2 and 11/2) respectively.

The radiative emission rates (A_{0-J}) of electric dipole related with J-O parameters was expressed as:

$$A_{(0-J)} = \frac{64\pi^4 \upsilon_J^{\ 3}}{3h(2J+1)} \frac{n(n^2+2)^2}{9} \sum_{J=2,4} \Omega_J \left| \left\langle ^5D_0 \left\| U^{(J)} \right\| ^7F_J \right\rangle \right|^2 \quad \text{------------------------- (15)}$$

where, e denotes electronic charge, υ_J is wavenumber of the corresponding transitions, h Planck's constant and n RI of the sample. $\left| \left\langle ^5D_0 \left\| U^{(J)} \right\| ^7F_J \right\rangle \right|^2$ shows squared reduced matrix elements of Dy^{3+} ions [36]. Thus, by using Eqs. (14) and (15), the values of Ω_2 and Ω_4 were estimated and are given in Table 3. The radiative transition probability (A_T), radiative lifetime (τ_{rad}) and branching ratio $\beta(\psi_J)$ were determined by using the relations [38];

$$A_T(\psi_J) = \sum_{J'} A_{J-J'} \text{ --------------- (16)}$$

$$\tau_{rad}(\psi_J) = \frac{1}{A_T(\psi_J)} \text{ ------------- (17)}$$

$$\beta(\psi_J) = \frac{A(\psi_J, \psi'_{J'})}{A_T(\psi_J)} \text{ ------------------ (18)}$$

Further, the stimulated emission cross-section (σ_e) was also evaluated by the following equation;

$$\sigma_e(\lambda_P) = \left[\frac{\lambda_P^4}{8\pi cn^2 \Delta\lambda_{eff}} \right] A_{J'-J} \text{ ------- (19)}$$

where λ_P is the emission peak wavelength corresponding transitions, c the velocity of light, $\Delta\lambda_{eff}$ the effective bandwidth of the emission transition, and n the refractive index of the host lattice.

The calculated values of radiative properties are tabulated in Table 3. The variation in Ω_2 values with Dy^{3+} concentration indicates the high sensitivity to the ligand environment. The Ω_2 and Ω_4 parameters are mainly ascribed to short range and long range effect due to covalency and structural deviations in the environment of the Dy^{3+} ions. Further, the measured branching ratio was found to be ~ 0.99 ≥ 0.50 which endorses that the prepared NPs can emit pure white light emission which can be effectively used in solid state lightning applications.

Generally, FP types have been described into three groups: (i) level 1 features were described by fingerprint ridge flow and general morphological information, (ii) level 2 features provide pattern matching followed detection of individual fingerprint ridges, (iii) level 3 features are defined as all attributes of a ridge, including shape, width, pores and curvature [39-41]. In order to inspect the suitability of optimized $Ca_2SiO_4:Dy^{3+}$ (3 mol%) NPs for visualization of LFPs, series of attempts have been made to visualize complex LFPs of the same donor on various non-porous substrates namely aluminum foil, glass, marble and wooden surfaces under normal light. Well defined ridge details enabling complete level 1, 2 and 3 details of FPs was observed (Fig.8) due to nano regime and better adhesive nature of the optimized sample. Further, complex LFP on aluminium foil was visualized by staining optimized sample under normal light by smooth brushing. Visualized LFPs can reveal defined ridge characteristics including complicated level 3 sweat pores with high sensitivity and less background hindrance. Fig. 9 shows the LFPs visualized on curved surfaces, namely, soft drink cans, spray bottle and tea glass cup under normal light. The detailed ridge characteristics including level 1-3 were clearly revealed without background hindrance. Further, the LFP visualized on aluminium surface under normal light exhibits various ridge characteristics, such as, ridge bifurcation, termination, dot, small ridge, island, ridge end, whorl, lake, and sweat pores were clearly distinguished (Fig.10).

Further, in order to know the selectivity of optimized sample, a series of controlled experiments were performed by using commercially available Fe_2O_3 and TiO_2 powders and are shown in Fig.11. Based on the obtained results, one can observe that LFPs visualized by prepared sample exhibit detailed ridge characteristics including levels 1 - 3 as compared to conventional ones. Table 4 shows the comparison of various parameters namely, method of synthesis, FP development techniques, excitation wavelength, type of surfaces, efficiency and toxicity of various powders with $Ca_2SiO_4:Dy^{3+}$ NPs [42-51]. Therefore, it was authorized that the probability for the recognition of the foremost ridge details (even sweat pores) of LFPs on various surfaces was well established by optimized $Ca_2SiO_4:Dy^{3+}$ (3 mol%) NPs. Therefore, aforementioned results display the possible usage of $Ca_2SiO_4:Dy^{3+}$ NPs fabricated via combustion synthesis route for advanced Forensic applications.

4. Conclusions

In summary, the $Ca_2SiO_4:Dy^{3+}$ (1 mol%–11 mol%) NPs were fabricated successfully by solution combustion method using ODH as fuel. The followed preparation method has several benefits such as low cost, energy efficiency, high production volume, simple method and high purity of the product. The crystallite size was estimated in the range 30–40 nm respectively. From SEM studies, the particles appear to be non-uniform and agglomerates are composed of circular with several micrometers in size. The optical band gaps for Dy^{3+} doped NPs were estimated to be in the range 5.19–5.30 eV. The obtained photometric results were on par with commercial white light with high purity. The optimized product was successfully explored as efficient labeling agent for visualizing LFPs on various surfaces including glass, aluminum foil, wooden surface and different color background papers under normal light. Owing to nano regime and good adherence efficiency, LFPs were visualized with high sensitivity, low background hindrance, high efficiency, and low toxicity. Further, for the first time well defined level 3 ridge details under normal light can be explored by simple powder dusting method. Therefore, the obtained NPs can be a definitive choice as advanced luminescent NPs for multifunctional applications.

References

1. Wang LY, Song EH, Zhou YY, Deng TT, Yea S, Zhang QY. Synthesis and warm-white LED applications of an efficient narrow-band red emitting phosphor, $Rb_2ZrF_6:Mn^{4+}$. *J Mater Chem C.* 2017; 5: 7253.

2. Xu W, Min XL, Chen X, Zhu YS, Zhou PW, Cui SB, et al. $Ag-SiO_2-Er_2O_3$ nanocomposites: Highly effective upconversion luminescence at high power excitation and high temperature. *Sci Rep.* 2014; 4: 5087.

3. Xu W, Min XL, Chen X, Zhu YS, Zhou PW, Cui SB, et al. Nd_2O_3/Au nanocomposites: upconversion broadband emission and enhancement under near-infrared light excitation. *J Mater Chem C*. 2012; 2: 5857.

4. Lu W, Xu HW, Huo JS, Shao BQ, Feng Y, Zhao S, et al. Tunable white light of a Ce^{3+}, Tb^{3+}, Mn^{2+} triply doped $Na_2Ca_3Si_2O_8$ phosphor for high colour-rendering white LED applications: tunable luminescence and energy transfer. *Dalton Trans.* 2017; 46: 9272.

5. Xiang GT, Ma Y, Zhou XJ, Jiang S, Li L, Luo XB, et al. Investigation of the energy-transfer mechanism in Ho^{3+}- and Yb^{3+}- codoped Lu_2O_3 phosphor with efficient near-infrared downconversion. *Inorg Chem.* 2017; 56: 1498.

6. Li F, Liu SQ, Qi RY, Li H, Cui TF. Effective visualization of latent fingerprints with red fluorescent $La_2(MoO_4)_3:Eu^{3+}$ microcrystals. *J Alloys Compd.* 2017; 727: 924.

7. Basavaraj RB, Nagabhushana H, Daruka Prasad B, Vijayakumar GR. Zinc silicates with tunable morphology by surfactant assisted sonochemical route suitable for NUV excitable white light emitting diodes. *Ultrason Sonochem.* 2017; 34: 700.

8. Basavaraj RB, Nagabhushana H, Daruka Prasad B, Sharma SC, Prashantha SC, Nagabhushana BM. A single host white light emitting $Zn_2SiO_4:Re^{3+}$ (Eu, Dy, Sm) phosphor for LED applications. *Optik.* 2015; 126: 1745.

9. Venkataravanappa M, Nagabhushana H, Darshan GP, Sharma SC, Archana KV, Basavaraj RB, Daruka Prasad B. Facile ultrasound route for the fabrication of green emitting $Ba_2SiO_4:Eu^{2+}$ nanophosphors for display and dosimetric applications. *Mater Res Bull.* 2018; 97: 281.

10. Nagabhushana H, Sunitha DV, Sharma SC, Daruka Prasad B, Nagabhushana BM, Chakradhar RPS. Enhanced luminescence by monovalent alkali metal ions in $Sr_2SiO_4:Eu^{3+}$ nanophosphor prepared by low temperature solution combustion method. *J Alloys Compd.* 2014; 595: 192.

11. Nagabhushana H, Sunitha DV, Sharma SC, Prashantha SC, Nagabhushana BM, Chakradhar RPS. $CdSiO_3$: Eu^{3+} red nanophosphors prepared by low temperature solution combustion technique, its structural and luminescent properties. *J Alloys Compd.* 2014; 616: 284.

12. Venkataravanappa M, Nagabhushana H, Daruka Prasad B, Darshan GP, Basavaraj RB, Vijayakumar GR. Dual color emitting Eu doped strontium orthosilicate phosphors synthesized by bio-template assisted ultrasound for solid state lightning and display applications. *Ultrason Sonochem.* 2017; 34: 803.

13. Manohar T, Prashantha SC, Ramachandra Naik, Nagabhushana H, Nagaswarupa HP, Anantharaju KS, Girish KM, Premkumar HB. A benign approach for tailoring the photometric properties and Judd-Ofelt analysis of $LaAlO_3$: Sm^{3+} nanophosphors for thermal sensor and WLED applications. *Sens Actuators: B.* 2017; 243: 1057.

14. Ramakrishna G, Ramachandra Naik, Nagabhushana H, Basavaraj RB, Prashantha SC, Sharma SC, Anantharaju KS. White light emission and energy transfer $(Dy^{3+} \rightarrow Eu^{3+})$ in combustion synthesized YSO: Dy^{3+}, Eu^{3+} nanophosphors. *Optik.* 2016; 127: 2939.

15. Ramakrishna G, Nagabhushana H, Basavaraj RB, Prashantha SC, Sharma SC, Ramachandra Naik, Anantharaju KS. Green synthesis, structural characterization and photoluminescence properties of Sm^{3+} co-doped Y_2SiO_5: Ce^{3+} nanophosphors for wLEDs. *Optik.* 2016; 127: 5310.

16. Venkataravanappa M, Nagabhushana H, Darshan GP, Daruka Prasad B, Vijayakumar GR, Premkumar HB, Udayabhanu. Novel EGCG assisted ultrasound synthesis of self-assembled Ca_2SiO_4: Eu^{3+} hierarchical superstructures: Photometric characteristics and LED applications. *Ultrason Sonochem.* 2016; 33: 226.

17. Wang M, Li M, Yu AY, Wu J, Mao CB. Rare Earth fluorescent nanomaterials for enhanced development of latent fingerprints. *ACS Appl Mater Interfaces.* 2015; 7: 28110.

18. Chen X, Xu W, Zhang LH, Bai X, Cui SB, Zhou DL, et al. Large upconversion enhancement in the "Islands" Au–Ag Alloy/$NaYF_4$: Yb^{3+}, Tm^{3+}/Er^{3+} composite films, and fingerprint identification. *Adv Funct Mater.* 2015; 25: 5462.

19. Zhou DL, Li DY, Zhou XY, Xu W, Chen X, Liu DL, et al. Semiconductor plasmon induced up-conversion enhancement in $mCu_{2-x}S@SiO_2@Y_2O_3$:Yb^{3+}/Er^{3+} core–shell nanocomposites. *ACS Appl Mater Interfaces.* 2017; 9: 35226.

20. Park JY, Yang HK. Novel red-emitting $Y_4Zr_3O_{12}$:Eu^{3+} nanophosphor for latent fingerprint technology. *Dyes Pigm.* 2017; 141: 348.

21. Darshan GP, Premkumar HB, Nagabhushana H, Sharma SC, Prashantha SC, Nagaswarupa HP, Daruka Prasad B. Blue light emitting ceramic nano-pigments of Tm^{3+} doped $YAlO_3$: Applications in latent finger print, anti-counterfeiting and porcelain stoneware. *Dyes Pigm.* 2016; 131: 268.

22. Saif M, Alsayed N, Mbarek A, El-Kemary M, Abdel-Mottaleb MSA. Preparation and characterization of new photoluminescent nano-powder based on Eu^{3+}: $La_2Ti_2O_7$ and dispersed into silica matrix for latent fingerprint detection. *J Mol Struct.* 2016; 1125:763.

23. Zhang XH, Lu ZM, Meng FB, Hu L, Xu XW, Lin J, et al. Luminescence properties of $Ca_3Si_2O_7$: Dy^{3+} phosphor for white light-emitting diodes. *Mater Lett.* 2012; 79: 292.

24. Darshan GP, Premkumar HB, Nagabhushana H, Sharma SC, Daruka Prasad B, Prashantha SC, Basavaraj RB. Superstructures of doped yttrium aluminates for luminescent and advanced forensic investigations. *J Alloys Compd.* 2016; 686: 577.

25. Munirathnam K, Dillip GR, Chaurasia S, Joo SW, P Raju BD, Sushma NJ. Investigations on surface chemical analysis using X-ray photoelectron spectroscopy and optical properties of Dy^{3+}-doped $LiNa_3P_2O_7$ phosphor. *J Mol Struct.* 2016; 118:117.

26. Darshan GP, Premkumar HB, Nagabhushana H, Sharma SC, Daruka Prasad B, Prashantha SC. Neodymium doped yttrium aluminate synthesis and optical properties–A blue light emitting nanophosphor and its use in advanced forensic analysis. *Dyes Pigm.* 2016; 134: 227.

27. Tsunekawa S, Wang J, Kawazoe Y, Kasuya A. Blue shifts in the ultraviolet absorption spectra of cerium oxide nanocrystallites. *J Appl Phys.* 2003; 94: 3654.

28. Suresh C, Nagabhushana H, Darshan GP, Basavaraj RB, Daruka Prasad B, Sharma SC, Sateesh MK, Shabaaz Begum JP. Lanthanum oxyfluoride nanostructures prepared by modified sonochemical method and their use in the fields of optoelectronics and biotechnology. *Arabian J Chem.* https://doi.org/10.1016/j.arabjc.2017.03.006.

29. Wan Y, Abudouwafu T, Yusufu T, He JY, Sidike A. Photoluminescence properties and energy transfer of a single-phased white-emitting $NaAlSiO_4:Ce^{3+}, Sm^{3+}$ phosphor. *J Rare Earths.* 2017; 35: 850.

30. Zhou JH, Yu X, Wang T, Zhou DC, Qiu JB. A single-phased white-emitting $Ca_2Ga_2GeO_7:Dy^{3+}$ phosphor with different charge compensation ions. *J Rare Earths.* 2017; 35: 241.

31. Vidya YS, Anantharaju KS, Nagabhushana H, Sharma SC, Nagaswarupa HP, Prashantha SC, Shivakumara C, Danith kumar. Combustion synthesized tetragonal $ZrO_2: Eu^{3+}$ nanophosphors: structural and photoluminescence studies. *Spectrochim Acta Part A.* 2015; 135: 241.

32. Kolesnikov IE, Mamonov DV, Lahderant E, Kurochkin AV, Mikhailov MD. The impact of doping concentration on structure and photoluminescence of $Lu_2O_3: Eu^{3+}$ nanocrystals. *J Lumin.* 2017; 187:26.

33. Liao TQ, Liu H, Hussin R, Ibrahim Z, Deraman K, Lintang HO, Shamsuri WNW. Effects of Eu^{3+} and Dy^{3+} doping or co-doping on optical and structural properties of $BaB_2Si_2O_8$ phosphor for white LED applications. *J Rare Earths.* 2016; 34: 21.

34. Liu QB, Liu YF, Yang ZP, Han Y, Li X, Fu GS. Multi-wavelength excited white-emitting phosphor Dy^{3+}-activated $Ba_3Bi(PO_4)_3$. *J Alloys Compd.* 2012; 515:16.

35. Venkatachalaiah KN, Nagabhushana H, Darshan GP, Basavaraj RB, Daruka Prasad B, Sharma SC. Structural, morphological and photometric properties of sonochemically synthesized Eu^{3+} doped Y_2O_3 nanophosphor for optoelectronic devices. *Mater Res Bull.* 2017; 94: 442.

36. Li J, Wang J, Yu Y, Zhu YN, Ge MQ. Preparation and luminescence properties of rare-earth doped fiber with spectral blue-shift: $SrAl_2O_4:Eu^{2+}, Dy^{3+}$ phosphors/triarylsulfonium hexafluoroantimonate based on polypropylene substrate. *J Rare Earths.* 2017; 35: 530-535.

37. Basavaraj RB, Nagabhushana H, Daruka Prasad B, Sharma SC, Venkatachalaiah KN. Mimosa pudica mediated praseodymium substituted calcium silicate nanostructures for white LED application. *J Alloys Compd.* 2017; 690: 730.

38. Shivram M, Prashantha SC, Nagabhushana H, Sharma SC, Thyagarajan K, Harikrishna R, Nagabhushana BM. Low temperature synthesis and photoluminescence properties. *Spec Chim Acta Part A: Mol Biomol Spec.*2014; 120:395.

39. Dhananjaya N, Nagabhushana H, Nagabhushana BM, Rudraswamy B, Shivakumara C, Chakradhar RPS. Effect of Li^+-ion on enhancement of photoluminescence in $Gd_2O_3:Eu^{3+}$ nanophosphors prepared by combustion technique. *J Alloys Compd*. 2011; 509: 2368.

40. Som S, Kunti AK, Kumar V, Kumar V, Dutta S, Chowdhury M, Sharma SK, Terblans JJ, Swart HC. Defect correlated fluorescent quenching and electron phonon coupling in the spectral transition of Eu^{3+} in $CaTiO_3$ for red emission in display application. *J Appl Phys.*2014; 115: 193101.

41. Du F, Nakai Y, Tsuboi T, Huang Y, Seo HJ. Luminescence properties and site occupations of Eu^{3+} ions doped in double phosphates $Ca_9R(PO_4)_7$ (R=Al, Lu). *J Mater Chem*. 2011; 21: 4669.

42. Liu XM, Li CX, Quan ZW, Cheng ZY, Lin J. Tunable luminescence properties of $CaIn_2O_4:Eu^{3+}$ phosphors. *J Phys Chem C*. 2007; 111: 16601.

43. Kim YJ, Jung HS, Lim J, Ryu SJ, Lee JK. Rapid imaging of latent fingerprints using biocompatible fluorescent silica nanoparticles. *Langmuir.*2016; 32: 8077.

44. Mondal K, Kumar P, Manam J. Influence of doping and annealing temperature on the structural and optical properties of Mg_2SiO_4: Eu^{3+} synthesized by combustion method. *Curr Appl Phys.* 2016; 16:707.

45. Deepthi NH, Darshan GP, Basavaraj RB, Daruka Prasad B, Nagabhushana H. Large-scale controlled bio-inspired fabrication of 3D $CeO_2:Eu^{3+}$ hierarchical structures for evaluation of highly sensitive visualization of latent fingerprints. *Sens Actuators: B*. 2018; 255: 3127.

46. Darshan GP, Premkumar HB, Nagabhushana H, Sharma SC, Prashantha SC, Daruka Prasad B. Effective fingerprint recognition technique using doped yttrium aluminate nano phosphor material. *J Colloid Interface Sci*. 2016; 464:206.

47. Fernandes D, Krysmann MJ, Kelarakis A. Carbogenically coated silica nanoparticles and their forensic applications. *Chem Commun*.2016; 52:8294.

48. Chen H, Ma RL, Chen Y, Fan LJ. Fluorescence development of latent fingerprint with conjugated polymer nanoparticles in aqueous colloidal solution. *ACS Appl Mater Interfaces.*2017; 9: 4908.

49. Fernandes D, Krysmann MJ, Kelarakis A. Carbon dot based nanopowders and their application for fingerprint recovery. *Chem Commun.*2015;51:4902

50. Sandhyarani A, Kokila MK, Darshan GP, Basavaraj RB, Daruka Prasad B, Sharma SC, Lakshmi TKS, Nagabhushana H. Versatile core-shell $SiO_2@ SrTiO_3:Eu^{3+}$, Li^+ nanopowders as fluorescent label for the visualization of latent fingerprints and anti-counterfeiting applications. *Chem Eng J.*2017; 327:1135.

51. Venkatachalaiah KN, Nagabhushana H, Darshan GP, Basavaraj RB, Daruka Prasad B. Novel and highly efficient red luminescent sensor based $SiO_2@Y_2O_3:Eu^{3+}$, M^+ (M^+ = Li, Na, K) composite core–shell fluorescent markers for latent fingerprint recognition, security ink and solid state lightning applications. *Sens Actuators: B*. 2017; 251:310.

52. Ramachandra Naik, Prashantha SC, Nagabhushana H. Effect of Li$^+$ co doping on structural and luminescent properties of Mg$_2$SiO$_4$: RE^{3+} (RE= Eu, Tb) nanophosphors for displays and eccrine latent fingerprint detection. *Opt Mater.*2017; 72: 295.

53. Basavaraj RB, Nagabhushana H, Darshan GP, Daruka Prasad B, Sharma SC, Venkatachalaiah KN. Ultrasound assisted rare earth doped Wollastonite nanopowders: Labeling agent for imaging eccrine latent fingerprints and cheiloscopy applications. *J Ind Eng Chem.* 2017; 51: 90.

54. Basavaraj RB, Nagabhushana H, Darshan GP, Daruka Prasad B, Rahul M, Sharma SC, Sudaramani R, Archana KV. Red and green emitting CTAB assisted CdSiO$_3$:Tb^{3+}/Eu^{3+} nanopowders as fluorescent labeling agents used in forensic and display applications. *Dyes Pigm.*2017; 147:364.

55. Dhanalakshmi M, Nagabhushana H, Darshan GP, Basavaraj RB, Daruka Prasad B. Sonochemically assisted hollow/solid BaTiO$_3$: Dy^{3+} microspheres and their applications in effective detection of latent fingerprints and lip prints. *J Sci: Adv Mater Devices.*2017; 2: 22.

Research Highlights

1. Novel $Ca_2SiO_4:Dy^{3+}$ NPs were prepared by solution combustion route.

2. LFPs visualized using optimized NPs is more effective with better resolution, detailed fingerprint ridges, easy fluorescence capture, and less background interference.

3. Level 1-3 ridge details were effectively visualized using optimized fluorescent labeling agent.

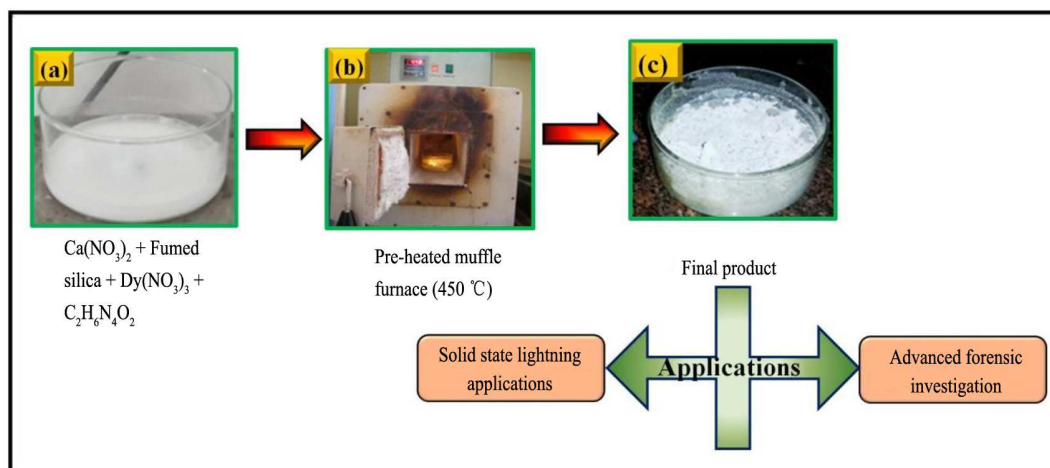4. The optimized product was used for forensic and solid state lightning applications.

Fig.1. Schematic illustration for the synthesis of Ca_2SiO_4:Dy^{3+} (1 mol%–11 mol%) NPs by solution combustion route.
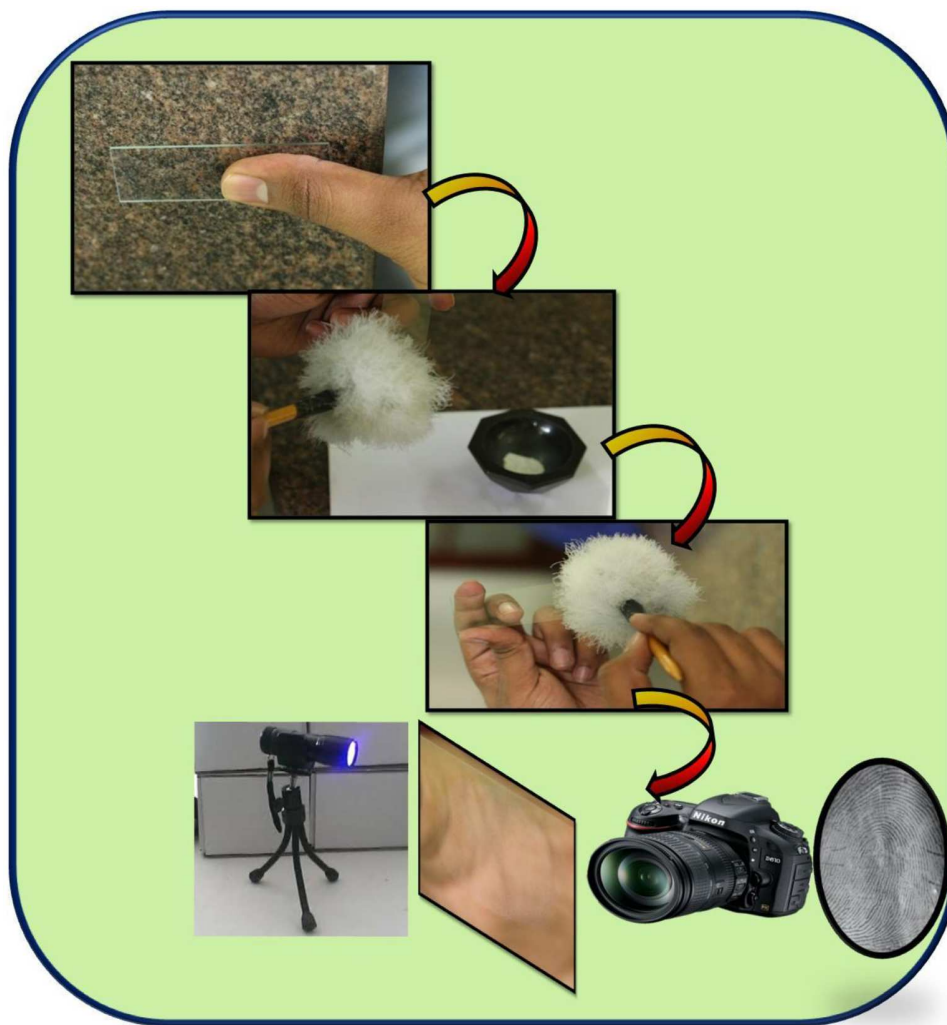
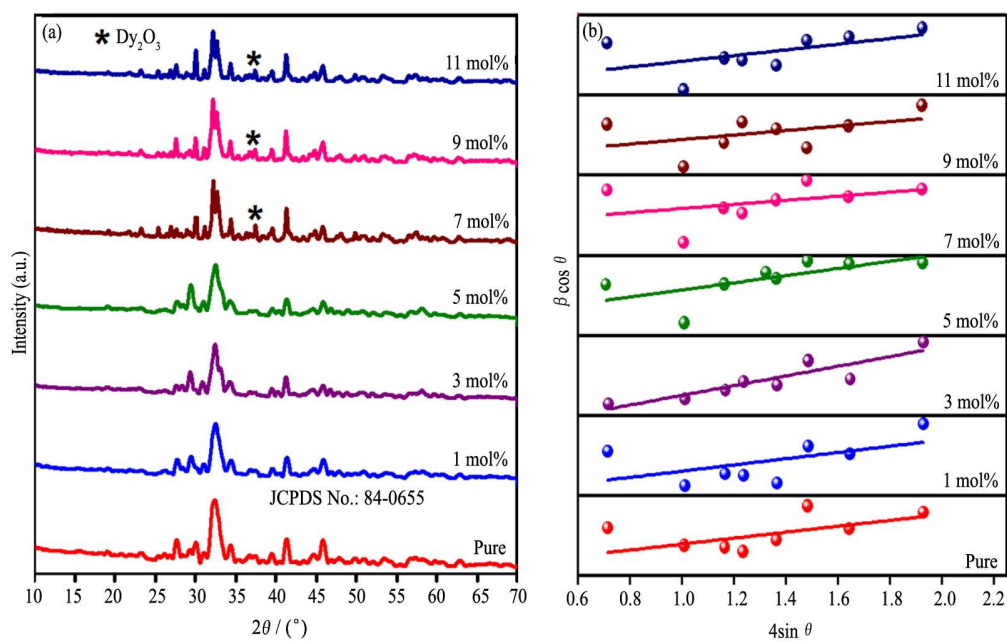Fig.2. Schematic illustration for the visualization of LFPs by staining Ca_2SiO_4:Dy^{3+} (3 mol%) NPs by powder dusting method.

Fig.3 PXRD patterns (a) and W-H plots (b) of pure and Dy^{3+} (1 mol%–11 mol%) doped Ca_2SiO_4 NPs.

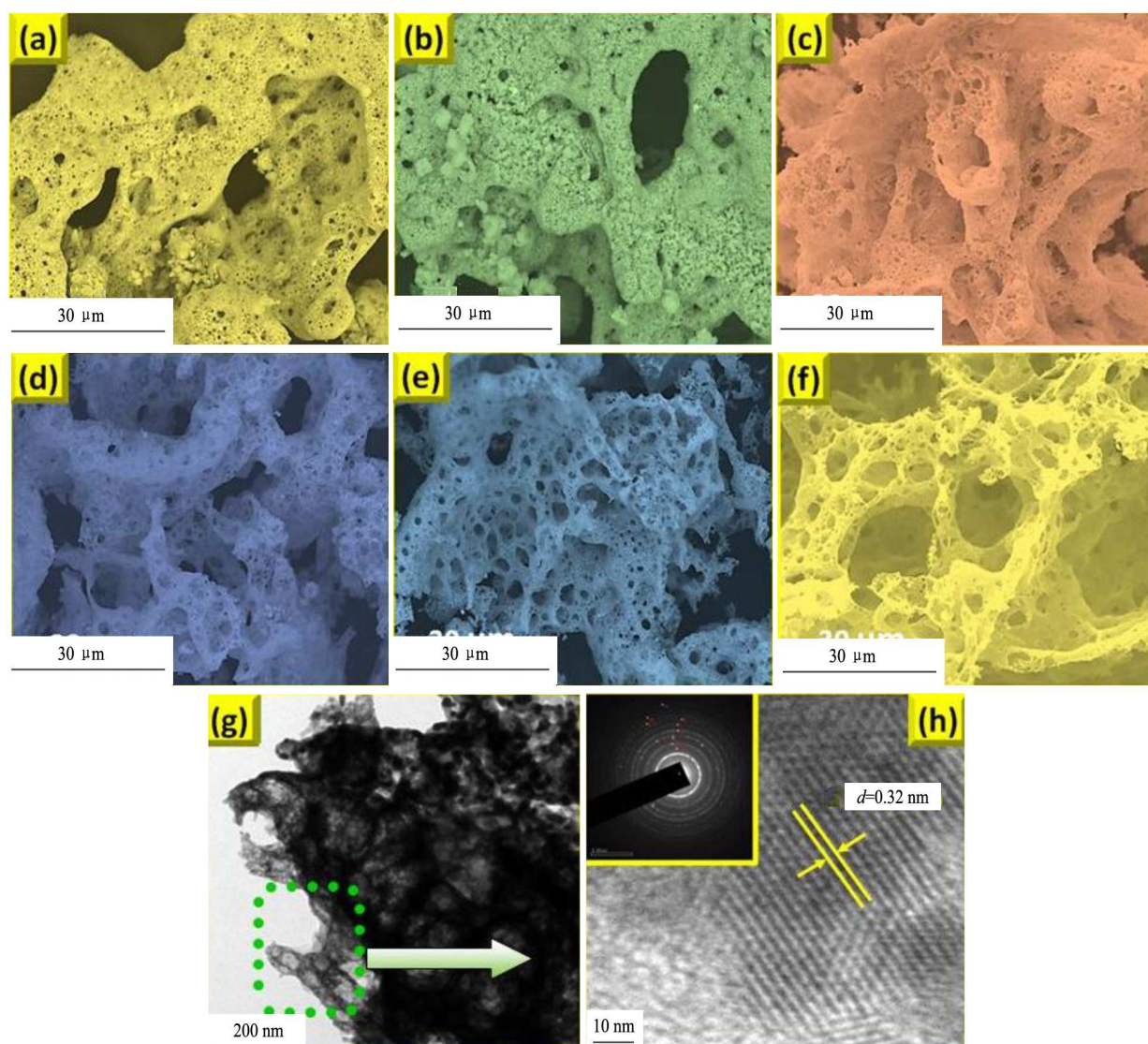Fig.4 SEM micrographs of Ca_2SiO_4:Dy^{3+} (1 mol%−11 mol%) NPs (a-f), TEM (g), HRTEM (h) images of Ca_2SiO_4:Dy^{3+} (3 mol%) NPs (Inset: SAED pattern).
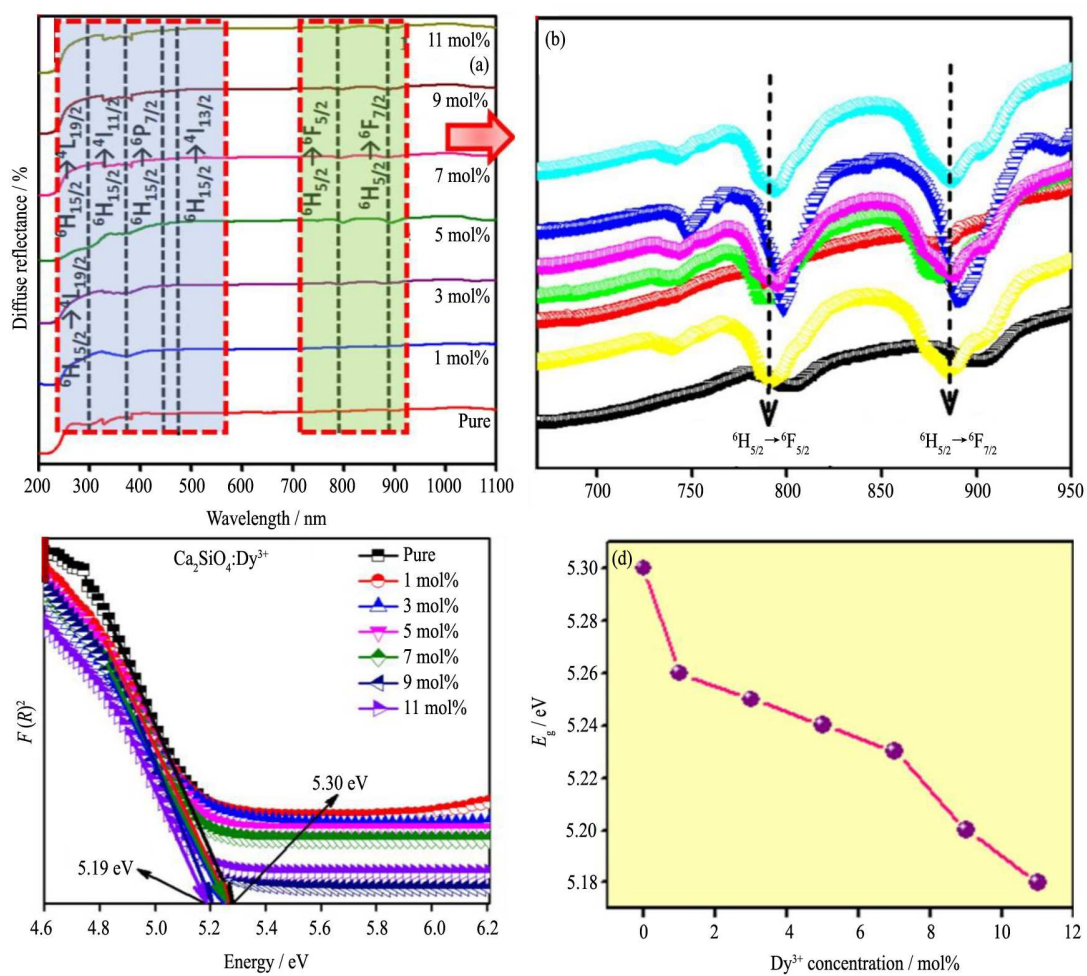
Fig.5 DR spectra (a), magnified view of 796 and 887 nm peaks (b), energy band gap plot (c) and variation of energy gap values with Dy^{3+} concentrations (d).
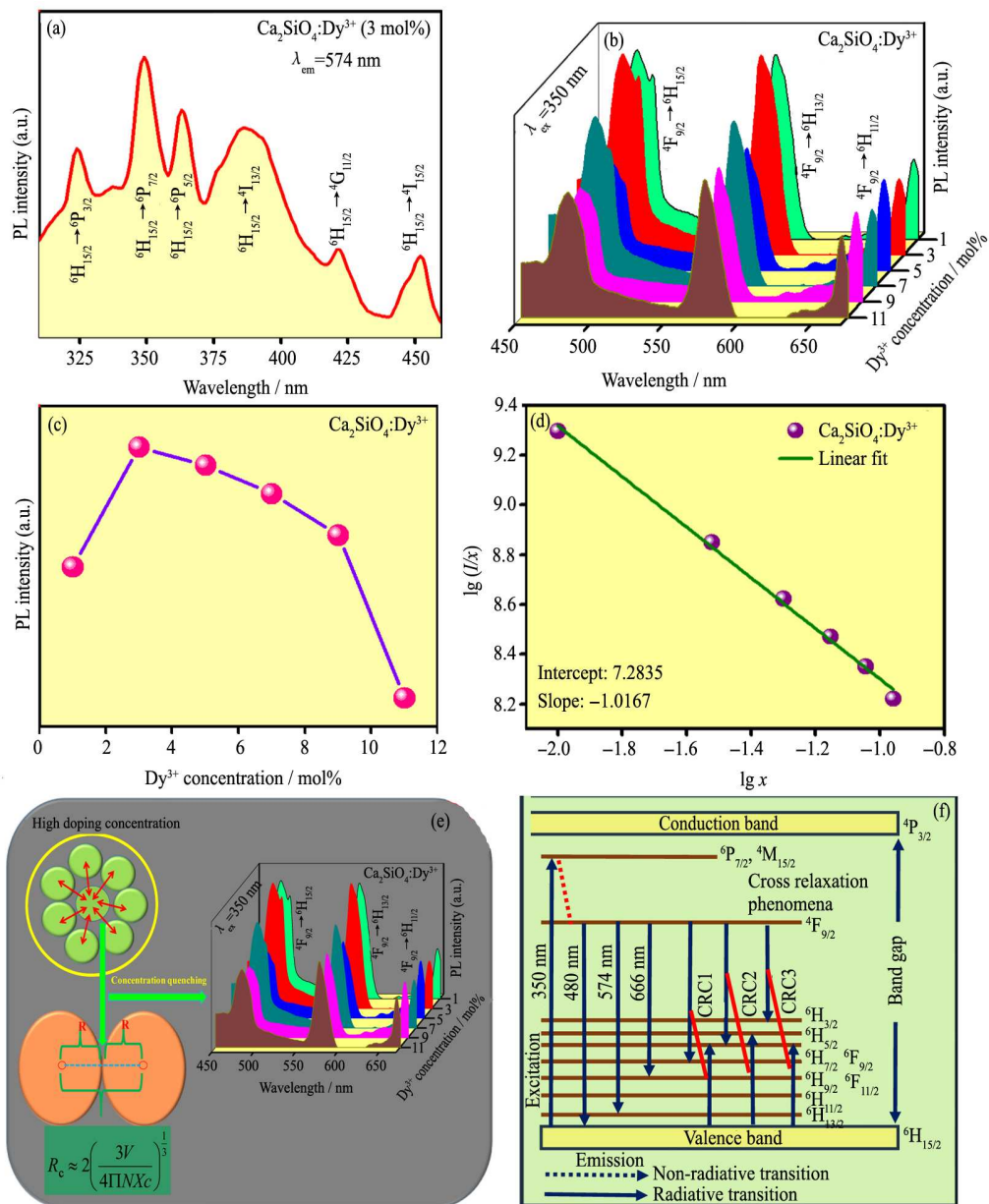
Fig.6 Excitation spectrum (a), emission spectra (b), PL intensity vs Dy^{3+} concentration (c), logarithmic plot of (x) vs (I/x) (d), schematic illustration of concentration quenching phenomena in $Ca_2SiO_4:Dy^{3+}$ NPs (e) and energy level diagram of Dy^{3+} ions in Ca_2SiO_4 host (f).
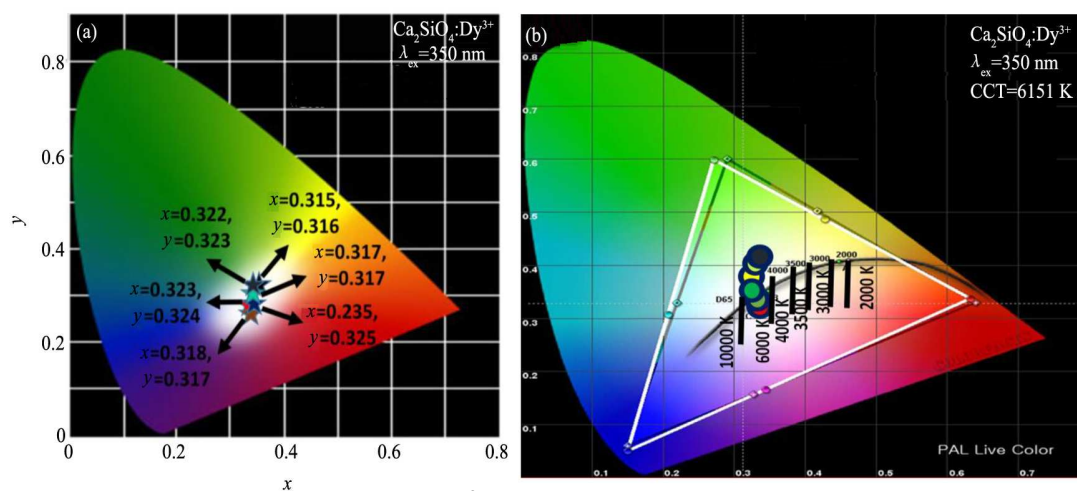
Fig.7 CIE (a) and CCT (b) diagrams of $Ca_2SiO_4:Dy^{3+}$ (1 mol%−11 mol%) NPs.
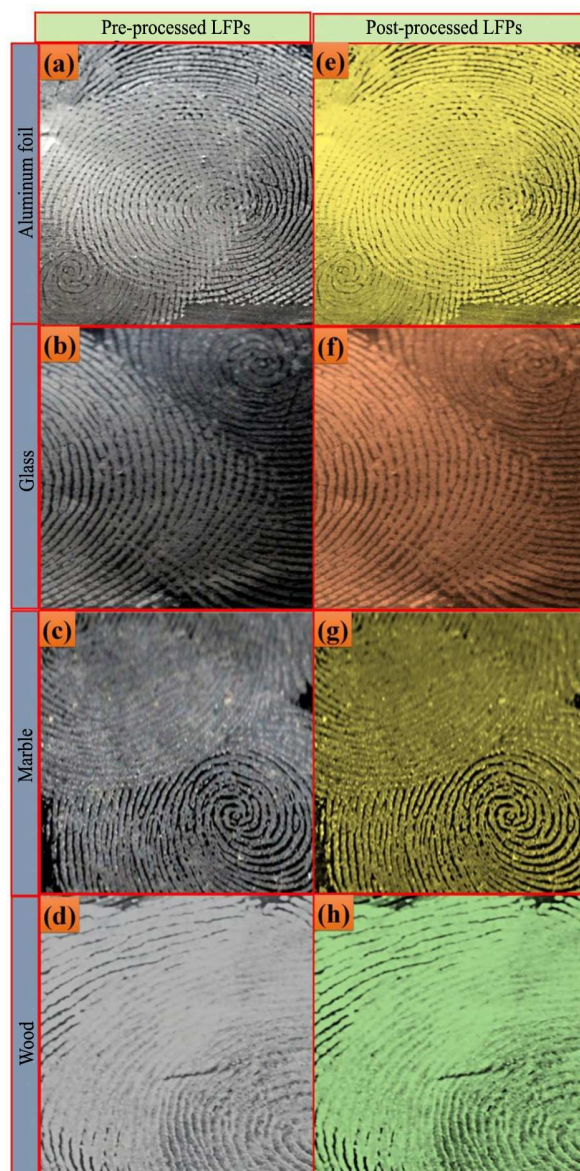
Fig.8. Pre - processed overlapped LFPs visualized by staining Ca_2SiO_4:Dy^{3+} (3 mol%) NPs on aluminum foil (a), glass (b), marble (c), wood surfaces (d) and post processed images (e–h).
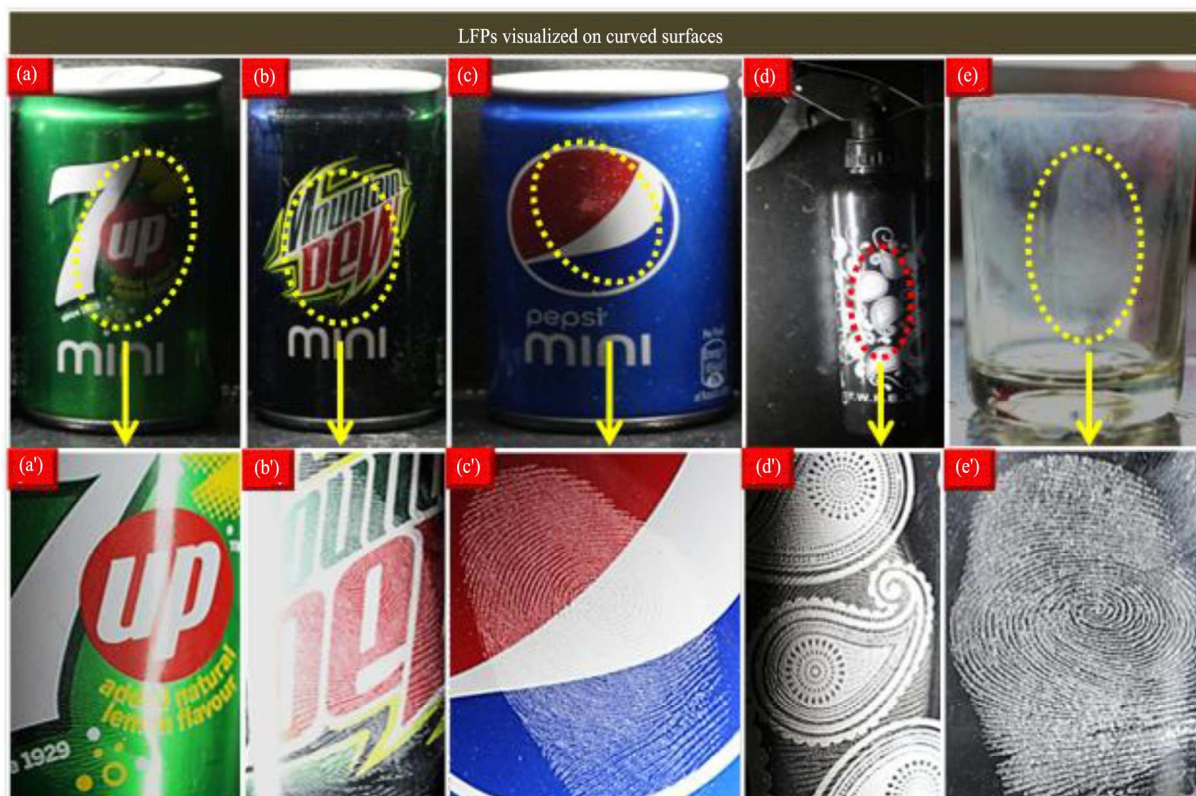
Fig.9 LFPs visualized under normal light on various curved surfaces (a-e) and enlarged images (a^1-e^1).
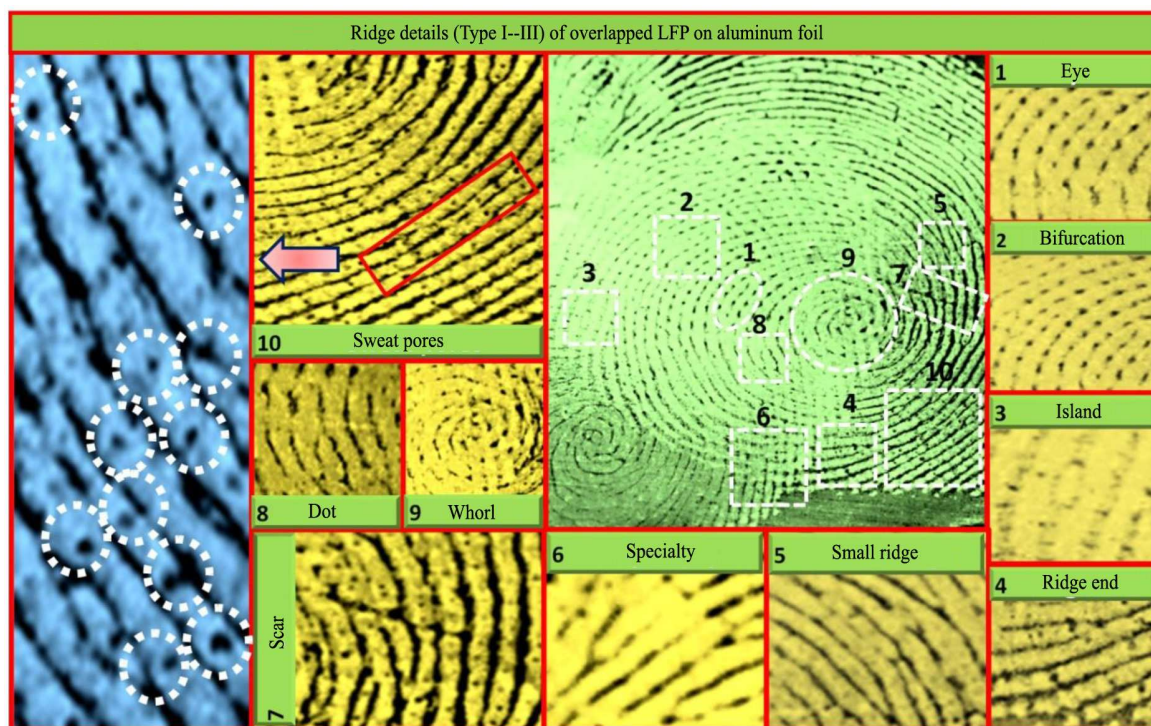
Fig.10. Well defined ridge details (Type 1-3) of overlapped LFP visualized by staining $Ca_2SiO_4:Dy^{3+}$ (3 mol%) NPs.

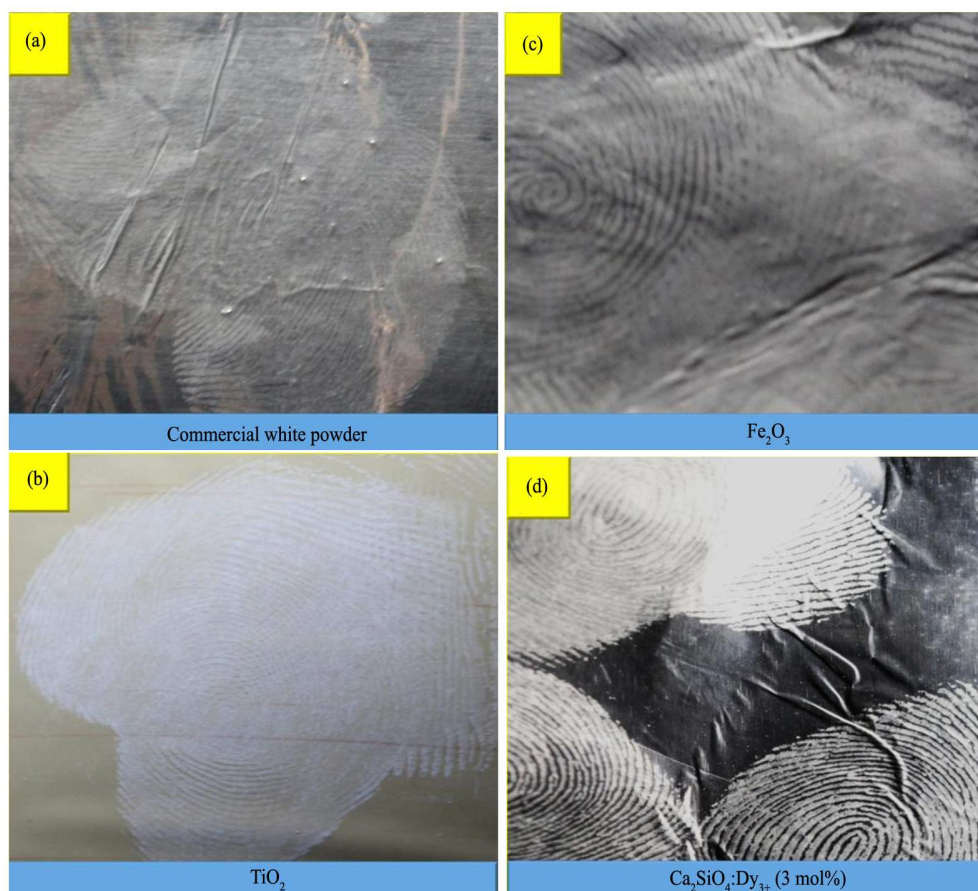Fig.11. Comparison between the visualized LFPs stained by commercial FP powders: (a) white powder; (b) TiO$_2$; (c) Fe$_2$O$_3$; (d) Ca$_2$SiO$_4$:Dy^{3+} (3 mol%) NPs.

Table 1: Bandey's FP grading scheme.

Grade	Description
0	No description
1	No continuous ridges; all discontinuous or dotty
2	One third of the mark comprised of continuous ridges; remainder either show no development or dotty
3	Two thirds of the mark comprised of continuous ridges; remainder either show no development or dotty
4	Full development; whole mark comprised of continuous ridges

Table 2: Estimated crystallite size, micro-strain, lattice strain, dislocation density and stacking fault of pure and Ca_2SiO_4:Dy^{3+} (1 mol%–11 mol%) NPs.

Ca_2SiO_4 : Dy^{3+} (mol%)	Average crystallite size d/nm		Micro-strain ε ($\times 10^{-3}$)	Lattice strain ϵ ($\times 10^{-3}$)	Dislocation density δ ($\times 10^{14}$ lin/m^2)	Stacking fault
	Scherrer's method	W-H plots				
pure	40	43	1.01	2.24	6.21	0.41
1	38	40	1.11	3.19	9.79	0.45
3	37	39	1.09	3.29	9.88	0.47
5	35	36	1.12	3.47	10.17	0.49
7	33	33	1.15	3.89	10.74	0.52
9	30	31	1.11	4.24	10.96	0.55
11	28	30	1.02	4.82	11.24	0.59

Table 3: J-O intensity parameters (Ω_2 & Ω_4), Emission peak wavelengths (λ_p), radiative transition probability (A_T), radiative lifetime (τ_{rad}), branching ratio (β_R), stimulated emission cross-section and quantum efficiency of $Ca_2SiO_4:Dy^{3+}$ (1 mol%–11 mol%) NPs

| $Ca_2SiO_4:Dy^{3+}$ conc. (mol%)	J-O parameters ($\times 10^{-20}$ cm^2)		λ_p (nm)	A_T (s^{-1})	τ_{rad} (ms)	β_R	$\sigma(\lambda_P)$ ($\times 10^{-22}$ cm^2)	η (%)
	Ω_2	Ω_4						
1	5.96	6.56	574	287.3	3.48	0.998	17.24	70.63
3	6.30	6.51	574	303.9	3.29	0.999	26.34	82.88
5	6.47	5.95	574	312.0	3.20	0.998	32.38	76.60
7	7.04	10.51	575	339.6	2.94	0.998	32.78	73.64
9	7.03	10.36	575	338.8	2.95	0.999	34.32	78.68
11	6.42	10.48	574	356.2	2.86	0.999	34.88	70.42

Table 4: Comparison of method of synthesis, FP technique, excitation wavelength, type of surfaces, efficiency and toxicity of various powders with $Ca_2SiO_4:Dy^{3+}$ NPs.

Sl. No	Material	Synthesis method	Fingerprint technique	Excitation wavelength	Type of surfaces		Efficiency (levels of detection)	Toxicity	Ref
					Porous	Non-porous			
1.	$YAlO_3:Sm^{3+}$	SC	PD	365 nm	Freshly cut leaf	Aluminum foil, glass, transparent plastic sheet, stainless steel,	Level I & II	Low-toxic	Darshan et al. [46]
2.	PR254@SiO_2@PVPs	Stober, allylation and hydrosilylation	PD	254 nm	–	Polystyrene, glass	Level I, II & III	Non-toxic	Kim et al. [43]
3.	C-SiO_2	carbogenic	PD	350, 395, 590 nm	–	Glass and polymer	Level I, II & III	Non-toxic	Fernandes et al, [47]
4.	Poly (p-phenylene vinylene) (PPV) nanoparticles	Modified Wessling	SI	Normal light and 365 nm	–	Adhesive tapes, aluminum foil, cover glass	Level II	Low-toxic	Chen et al, [48]
5.	C-dot/silica NPs	carbogenic	PD	350, 380, 410, 440, 470 nm	Soft drink bottle foil	Glass slide,	Level I & II	Non-toxic	Fernandes et al, [49]
6.	SiO_2@$SrTiO_3$:Eu^{3+},L^{i+}	Stober and combustion	PD	254 nm	Currency, paper cup, magazine cover	Marble, metal foil, marker, remote, spatula, coin etc.	Level I, II & III	Non-toxic	Sandhyarani et al, [50]
7.	SiO_2@Y_2O_3:Eu^{3+}, M^+ (M^+ = Li, Na, K)	Stober and combustion	PD	254 nm	Currency, paper cup, magazine cover, credit cards	Scissor, marble, coin, CD, pellet die set etc.	Level I, II & III	Low-toxic	Venkatachalaiah et al, [51]
8.	$Mg_2SiO_4:RE^{3+}$ (RE = Eu, Tb)	SC	PD	254 nm	-	Aluminum foil, remote, stapler	Level I & II	Non-toxic	Ramachandra et al, [52]
9.	$CdSiO_3:Dy^{3+}$	SCS	PD	Normal light and 254 nm	Magazine cover, news paper	Marble, coin, CD, aluminum foil	Level I & II	Non-toxic	Basavaraj et al, [53]
10.	$CdSiO_3$:Tb^{3+}/Eu^{3+}	SCS	PD	254 nm	Magazine cover, plastic cover,	Marble, CD, aluminum foil, spatula, remote mobile etc.	Level I & II	Non-toxic	Basavaraj et al, [54]

					currency note				
11.	BaTiO$_3$:Dy^{3+}	SCS	PD	Normal light	-	Marble, pen, remote, coin etc.	Level I & II	Non-toxic	Dhanalakshmi et al, [55]
12.	Ca$_2$SiO$_4$:Dy^{3+}	SC	PD	Normal light	-	Foil, glass, marble and wood	Level I, II & III ridge details visualized in individual and overlapped FPs	Non-toxic	Present study

SC: Solution combustion, **SCS:** sonochemical synthesis, **PD:** Powder dusting, **SI:** Solution immersion

Graphical abstract
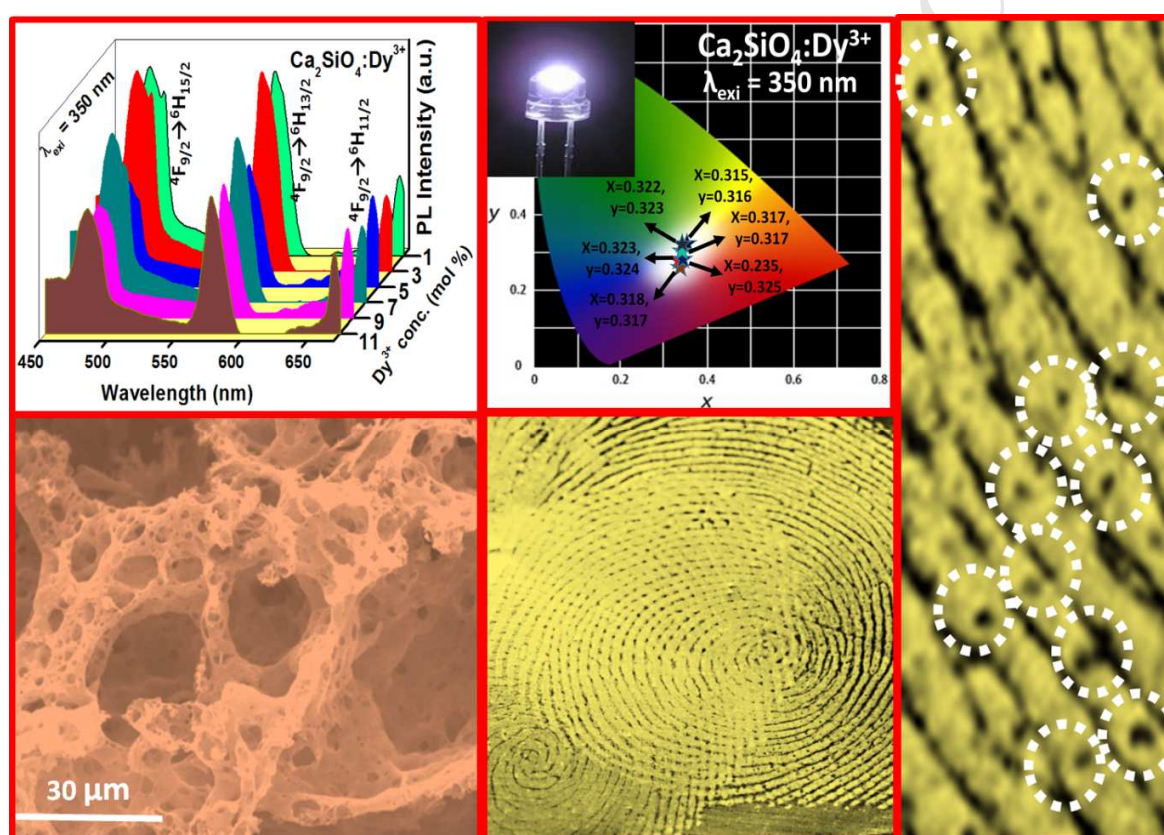
Comments table

Ms. Ref. No.: JRE-D-17-00404
Title: Multifunctional Dy (III) doped di-calcium silicate array for boosting display and forensic   applications
Journal of Rare Earths

	Reviewer #1	
1.	The term "rare earth" in the title should be replaced by "Dy(III)" for accuracy.	As per reviewer comment, we have included Dy (III) in the title of

		revised manuscript.
2.	The authors claim that their powder have the distinct advantage to reveal enhanced fingerprints under visible light, while other types of materials require the use of UV light. The authors should extend their comparison with other types of nanostructured fingerprint powders such as those described in: i. Journal of Colloid and Interface Science, 2016,464, 206 ii. Langmuir, 2016, 32, 8077 iii. Chem. Commun., 2016, 52, 8294 iv. ACS Appl. Mater. Interfaces, 2017, 9, 4908 v. Chem. Commun. 2015, 51, 4902 in terms of their cost, toxicity, efficiency, adhesion etc.	As per reviewer comment, the suggested references (Table.4) have been included and compared their cost, toxicity, efficiency, adhesion etc, with the present powder in the revised manuscript.
	Reviewer #2	
1.	The author should review the rare earth doped white LEDs materials and fingerprints based on rare earth doped materials in detail, and providing the advantage of $Ca_2SiO_4:Dy^{3+}$ nanopowders in the introduction part. I suggest the authors to refer and cite the related papers, such as Scientific Reports 4, 5087 (2014); Journal of Materials Chemistry C 2 (29), 5857-5863; Advanced Functional Materials, 25 (2015) 5462-5471 ; ACS Applied Materials & Interfaces 9 (40), 35226-35233.	As per reviewer comment, we have included suggested references in the introduction part of the revised manuscript.
2.	The Dy^{3+} ions doping concentration reached to 11% in the host, where did not show any impurity peak in XRD. Please providing the discussion about the location of Dy^{3+} ions in the host, where the valence state of Ca is $^{+2}$ and Si is $^{+4}$.	As per reviewer comment, Dy_2O_3 impurity peak positioned at $2\theta=36^o$ has been assigned in the PXRD profiles. In the present work, Dy^{3+} ions are effectively substituted in the Ca^{2+} site in the host and same is included in the revised manuscript.
3.	Deeply discussion about the energy band gap of the host decreased with increasing the Dy^{3+} doping concentration should be provided.	As per reviewer comment, the details of variation of energy band gap of the host decreased with increasing the Dy^{3+} doping concentration was included in the revised manuscript.
4.	In the sentence "It implies that the non-radiative energy transfer was responsible for energy transfer among Tb^{3+} ions due to multipole - multipole", there showed "Tb^{3+} ions". Does it mean Dy^{3+} ions? I suggest the author check the text carefully.	As per reviewer comment, we have rectified the mistake and replaced "Tb^{3+} ions" as "Dy^{3+} ions" in the revised manuscript.
5.	Please provide the emission efficiency of $Ca_2SiO_4:Dy^{3+}$ nanopowders.	As per reviewer comment, quantum efficiency of $Ca_2SiO_4:Dy^{3+}$ nanopowders have been studied using PL and included in the revised manuscript.
6.	Did you try the fingerprint on the bend substrate?	As per reviewer suggestion, LFP visualized on bend surfaces and details are given in the revised manuscript.